Research Article

Study on Method of Doping Au Nanoparticles on ZnO Stratified Microstructure to Enhance Photocatalytic Ability and Antibacterial Activity

Anh-Tuan Vu*, Thi Anh Tuyet Pham

School of Chemical Engineering, Hanoi University of Science and Technology, Hanoi, Vietnam.

Abstract

In this study, stratified microstructure gold/zinc oxide (Au/ZnO) composites were successfully prepared by the method of dispersing Au nanoparticles (Au NPs) on the surface of the hierarchical flower ZnO via $HAuCl_4$ reduction in the presence of different reducing agents such as sodium citrate (SC), sodium borohydride (SB), sodium hydroxide and ethanol (SE), and Hg lamp 250W. Au-doped samples were named Au/ZnO-SC, Au/ZnO-SB, Au/ZnO-SE, and Au/ZnO-Hg lamp, respectively. Au/ZnO-SC and Au/ZnO-SB revealed the uniform distribution of Au nanoparticles on the ZnO substrate, meanwhile, Au nanoparticles were very densely distributed in Au/ZnO-SE and Au/ZnO-Hg lamp samples. The pure ZnO only showed an absorption peak in the ultraviolet (UV) region, Au/ZnO samples indicated additional absorption peaks in the visible light region (500-600 nm), which were characteristic of the surface plasmon resonance (SPR) effect of Au NPs in composites. Therefore, their bandgap energy was reduced compared to ZnO (3.202 eV), leading to increased photocatalytic efficiency under visible light irradiation. Among the doped samples, Au/ZnO-SC (with Au content as 5 wt%) had the largest surface area (26.23 m^2/g) and the highest pore volume (0.263 cm^3/g) and average pore width (33.2 nm). As a result, it showed the highest catalytic efficiency through complete degradation of tartrazine (TA) within 30 min with a reaction rate of 0.124 min^{-1} under Hg lamp 250 irradiation. In addition, both pure ZnO and Au/ZnO nanocomposites exhibited high antimicrobial activity in killing *Escherichia coli (E. coli)*, and their enhancing effect of them was reliant on the weight ratio of Au on ZnO and the concentration of tested samples. These results indicated that Au/ZnO material has prominent potential for applications in water environment treatment.

1. Introduction

In the last few decades, the intense development of economic-technical activities has made people's lives more and more improved. Still, the downside of that is the release of numerous toxic substances into the environment. As a result, humans face climate change, environmental pollution, ecological imbalance, and the development of diseases. Water pollution is one of the most alarming issues [1]. Toxic organic and biological contaminants in wastewater increase carcinogenicity that threatens the life of humans. In particular, it is increasingly common that using large quantities of dyes containing insoluble functional groups such as naphthalene, phenolic, azo, amine, sulfonate, and thiol

* Corresponding Author.
  Email: tuan.vuanh@hust.edu.vn (A.-T. Vu);
  Phone: +84-912911902, Fax +84-0243 868 0070

in the food, textile, and paint industries can be able to cause detrimental impacts like discoloration, odor, bioaccumulation [2]. Hence, it is essential to figure out whether combinational remediation can address organic and biological contaminants.

Many efforts have been made to neutralize the harmful effects of wastewater caused by organic pollutants and infectious microorganisms. To treat persistent organic contaminants, advanced oxidation processes (AOPs) consisting of photocatalysis, electrochemical oxidation, or oxidation by Fenton system have been successful and widely applied methods currently since they are much more likely to completely decompose pollutants into innocuous substances such as CO_2 and H_2O [3,4]. Which, utilization of nanometal oxides is a potential research direction, and it has attracted a tremendous amount of interest from scientists [5]. In this regard, nanomaterials assume a role as photocatalysts which are likely to absorb irradiation to produce reactive oxygen species (ROS), degrading organic pollutants. Additionally, photocatalysis is considered an advanced technique and is being widely used to date because it can create a safe, sustainable, environmentally friendly, and cost-effective wastewater treatment method [6,7]. It plays a crucial role in their operations. Furthermore, with specific biological properties, several nanomaterials also can be able to antibacterial activity.

Since its advantages like mechanical stability and specific photoelectric properties [8], the ZnO-based material is commonly used as a catalyst for the decomposition of organic matter and removal of heavy metal in wastewater from industrial and agricultural fields [6,9–11]. However, the large bandgap energy is the limit of ZnO in absorbing visible light. Moreover, the propensity of rapid recombination of electrons and holes leads to reducing the quantum yield of ZnO, and the catalytic ability only remains for a short time. Recently, improving the catalytic efficiency in the visible region and reducing the recombination rate are the strategies of scientists.

In research with supporters, the graphene oxide/zinc oxide (GO-ZnO) composite prepared by the hydrothermal method could improve the photodegradation of phenol in visible light [10]. The chitosan/ZnO nanocomposite prepared by the eco-friendly method using *S. lycopersicum* leaf exhibited antibacterial activity against also the degradation of congo red under solar light, the degradation efficiency archived at 80% in 300 min. ZnO nanorods immobilized on kaoline exhibited the reduction efficiency for Cr(VI) of

approximately 88.0%, being much more effective than the bare ZnO (43.7%) [12]. The deposition of ZnO on g-C_3N_4 could generate the heterojunction structure and inhibit the recombination of electron-hole pairs. As a result, the CO_2 conversion on the ZnO/g-C_3N_4 composite was improved to the rate of 45.6 $\mu mol.h^{-1}.gcat^{-1}$ [13]. Simultaneous dispersion of Ag and mesoporous graphitic C_3N_4 on the ZnO plate shows effective degradation of Direct Orange 26 dye under ultraviolet (UV) light illumination. The best photocatalytic efficiency achieved 94% at 10 mg/L DO26, and pH = 6 in 120 min of reaction time [14]. ZnO-dope noble metal is a potential approach to address the drawbacks of ZnO through enhancement of the mobility of electrons and holes, inhibition of the recombination between them, and extension of absorption in the visible irradiation region of ZnO [15–20]. Besides, transition metal-doped ZnO nanoparticles were successfully prepared via a simple solvothermal route. In which, Cu^{2+} ions in the doped ZnO NPs acted as effective trappers to promote the photogenerated carriers separation efficiency and inhibit their recombination thereby enhancing photocatalytic activity [21]. On the other hand, the biaxial strains can significantly modulate the band gaps and band arrangement of the catalyst heterostructures, and all the strain heterostructures are beneficial for the absorption of visible light. The induced integrated electric field on the heterostructure interface can reduce the photochemical carrier recombination rate, which is favorable for improving the photocatalytic performance of ZnO/GeC [22]. However, these studies have also demonstrated that the catalytic performance of ZnO composites was greatly influenced by their morphology, size, and physical properties.

In research with supporters, ZnO is also considered a promising materials agent due to its good thermal stability, high antimicrobial activity, and excellent biocompatibility [23]. There are numerous reports on the biocidal nature of ZnO against different strains of bacteria such as *Staphylococcus aureus* (*S. aureus*) and *Escherichia coli* (*E. coli*) [24–27]. An increase in antibacterial could be created when precious metals were added to ZnO [28–30]. This application of them has initiated a positive development to resolve microbial resistance issues, leading to arouse extensive attention in the biomedical field, especially in cancer treatment.

From the above, it can be seen that the decoration of precious metal nanoparticles on the surface of ZnO is truly a potential method not only enhanced the degradation efficiency of or-

ganic pollutants under solar light but also increase their sterilization capacity. The morphology and dispersion of precious metal nanoparticles in composites, controlled by synthesis methods, will significantly influence their photocatalytic and bactericidal properties. In this study, the effect of the synthesis methods on physical properties, catalytic performance, and antibacterial activity of stratified microstructure Au/ZnO composite was throughout investigated. The different agents such as sodium citrate, sodium borohydride, sodium hydroxide, and light irradiation of Hg lamp 250W were selected for reducing agents. The catalytic performance of as-synthesized materials was evaluated by photocatalytic degrading tartrazine (TA) under visible irradiation. TA was selected as the organic substance in this study for its properties. First, TA is a typical substance that is widely used in areas such as food, textiles, and cosmetics. Next, it is confirmed to be highly toxic for humans since it is much more likely to cause asthma, eczema, thyroid cancer, and some other serious diseases [9]. Besides, the antibacterial ability of the as-prepared products was also evaluated by the agar plate diffusion method and using *E. coli* bacteria, a very common intestinal bacteria existing in wastewater.

2. Materials and Methods

2.1 Materials

Zinc nitrate hexahydrate ($Zn(NO_3)_2.6H_2O$, 99.5%), urea ($(NH_2)_2CO$, 99.5%), gold (III) chloride trihydrate ($HAuCl_4.3H_2O$), sodium citrate ($Na_3C_6H_5O_7$), sodium borohydride ($NaBH_4$), sodium hydroxide ($NaOH$), acid hydrochloric (HCl) and ethanol (C_2H_5OH) were purchased from Merck. tartrazine (TA) (99%), janus green B (JGB) (99%), congo red (CR) (99%) and methylene blue (MB) (99%) were obtained from Sigma-Aldrich.

2.2 Synthesis of the stratified ZnO

The ZnO stratified microstructure was fabricated by a simple hydrothermal process [6]. With this synthesis method, urea plays a crucial role in the formation of structuring ZnO. When urea was dispersed into the Zn^{2+} solution, the urea molecules were slowly hydrolyzed to release ammonia and CO_2. It was followed by the formation of OH^- and CO_3^{2-} anions, which can react with the Zn^{2+} ions to produce zinc carbonate hydroxide ($Zn_4(CO_3)(OH)_6$). After calcination, $Zn_4(CO_3)(OH)_6$ was decomposed and yielded ZnO powder. The rates of crystal nucleation and crystal formation determined the stratified structure of ZnO.

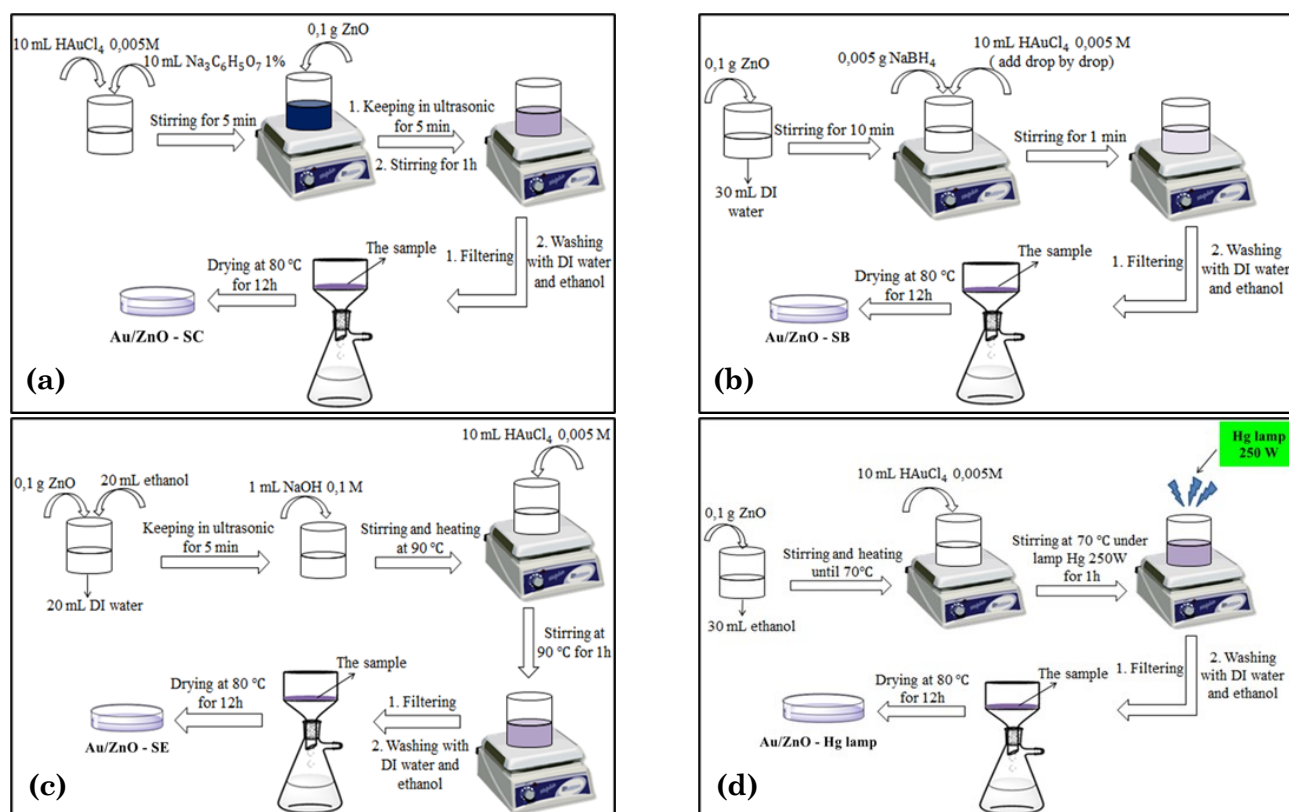Figure 1. The synthesis process of (a) Au/ZnO-SC; (b) Au/ZnO-SB; (c) Au/ZnO-SE and (d) Au/ZnO-Hg lamp.

Typically, 1.8018 g of $Zn(NO_3)_2$ was completely dissolved into 100 mL of distilled water before adding 0.03 moles of $(NH_2)_2CO$. The mixture was stirred for 30 min at 240 rpm/min. Subsequently, it was transferred to an autoclave, and heated to 90 °C for 24 h. As the autoclave was cooled, the white precipitate was filtered, washed with distilled water several times, and then dried at 90 °C for 24 h. Eventually, the ZnO sample was obtained after sintering the precipitate at 400 °C for 2 h with a heating rate of 2 °C/min.

2.3 Synthesis of stratified Au/ZnO composites

Method 1: First, 10 mL of 0.005 M $HAuCl_4$ and 10 mL of 1% $Na_3C_6H_5O_7$ were mixed in a beaker. Continuously, 0.1 g of ZnO was added into the mixture under stirring for 1 h. The precipitate was filtered by distilled water to remove impurity ions. After drying the sample at 80 °C for 12 h, the composite was obtained and named Au/ZnO-SC. The synthesis process is shown in Figure 1(a).

Method 2: Typically, 0.1 g of ZnO and 30 mL of distilled water were mixed together in a beaker. Thereafter, 0.002 g of $NaBH_4$ and 10 mL of 0.005 M $HAuCl_4$ solution were added into the white suspension drop by drop under stirring for 1 h with a constant speed to ensure good dispersion of the Au nanoparticles on the surface of ZnO. The composite was collected by vacuum pumping filtration with water and ethanol several. After drying in the air at 80 °C for 12 h, the purple composite was obtained and named Au/ZnO-SB. The synthesis process is shown in Figure 1(b).

Method 3: 0.1 g of ZnO, 20 mL of distilled water, and 20 mL of ethanol were mixed in a beaker by stirring for 5 min. 1 mL of 0.1 M NaOH was added to the mixture at a temperature of 90 °C, and 10 mL of 0.005 M $HAuCl_4$ was then added into the mixture under continuous stirring for 1 h. The product was filtered by distilled water and then dried at 80 °C for 12 h. The obtained composite was named Au/ZnO-SE. The synthesis process is shown in Figure 1(c).

Method 4: 0.1 g of ZnO and 30 mL ethanol were mixed by ultrasonic in 5 min. When the temperature increased to 70 °C, 10 mL of 0.005 M $HAuCl_4$ solution was added to the mixture. Then, the Hg lamp 250 W was turned on to allow the reduction process to take place. Finally, the precipitate was filtered by distilled water and dried in the air at 80 °C for 12 h. The obtained composite was named Au/ZnO-Hg lamp. The synthesis process is shown in Figure 1(d).

2.4 Characterizations

X-ray diffraction (XRD) method was recorded on a Bruker D8 Advance (Germany) with Cu Kα radiation (40 kV, 40 mA), 2θ angle from 10 to 80° was selected for analyzing the crystalline phase of composites. Transmission electron microscopy (TEM) and scanning electron microscopy (FE-SEM) methods were recorded on the JEM-2010 and JEOL-7600F instruments, respectively, for morphological observations of materials. The textural properties of composites were measured via the N_2 adsorption/desorption isotherm by micrometry (Gemini VII). The specific surface areas were calculated by the Brunauer-Emmett-Teller (BET) method, and the pore volume and diameter were determined by the BJH method. The Ultraviolet–visible diffuse reflectance (DR/UV-vis) spectra of the samples were measured on a UV-Vis spectrophotometer (Avantes). The Fourier transform infrared spectroscopy (FTIR, Madison, WI, USA) measurement was carried out to explore the changes in functional groups of as-synthesized samples by Nicolet IS50.

2.5 Experiment of photocatalytic reaction

The photocatalytic efficiency of composites was evaluated via the degradation of non-biodegradable toxic organic contaminants (TA, MB, JGB, and CR) under visible light. In the reactor, 100 mL solution containing the tested contaminant with a defined concentration were added by pH by HCl and NaOH solutions to reach a desired pH. A suitable amount of catalyst was introduced into the reactor and dispersed by the sonication for 5 min. After reaching adsorption/desorption equilibrium in the dark for 30 min, the light was turned on using Hg lamp 250 W (OSRAM 250 W-230 V, HWL, the light intensity of 13350 Lux), UV lamp 15 W (E27, the light intensity of 4710 Lux), or direct by solar light (light intensity of 82600 LUX). The concentrations of organic pollutants at each time interval were monitored by the UV-Vis spectrophotometer (Agilent 8453 instrument). The rate constant was calculated by using the pseudo-first-order model, equation (1) [31]. The degradation efficiency (DE) degradation capacity (DC) of the pollutant was determined by Equations (2) and (3) [31]. The crystal sizes samples were determined through equation (4) [32].

$$\ln\left(\frac{C_0}{C_t}\right) = kt \qquad (1)$$

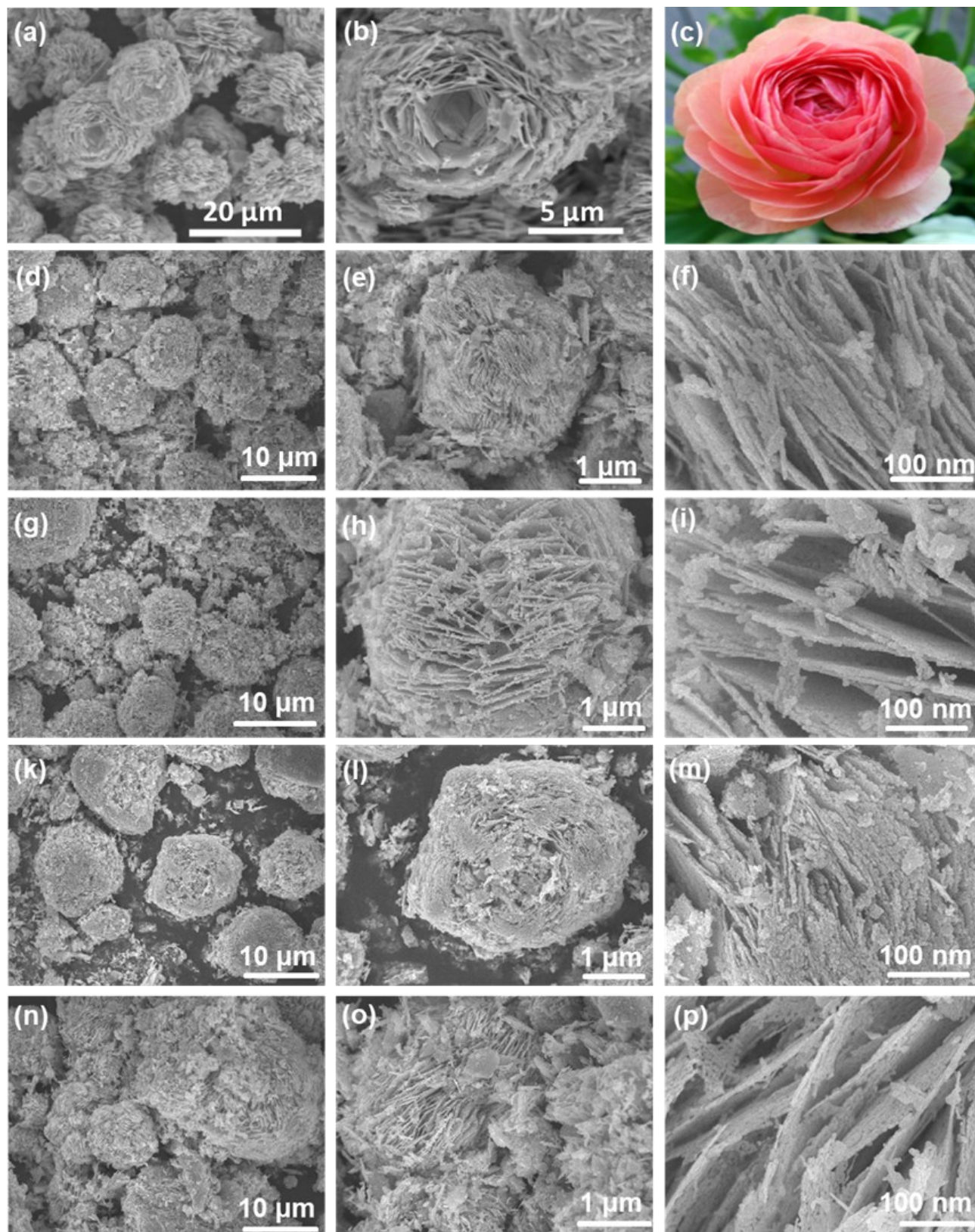$$DE(\%) = \frac{(C_0 - C_t) \times t}{C_0} \qquad (2)$$

Figure 2. SEM images of hierarchical Au/ZnO nanostructure with different scale bars of (a-c) hierarchical nanostructure; (d-f) hierarchical Au/ZnO-SC nanostructure; (g-i) hierarchical Au/ZnO-SB nanostructure; (k-m) hierarchical Au/ZnO-SE nanostructure and (n-p) hierarchical Au/ZnO-Hg lamp.

$$DC(mg/g) = \frac{(C_0 - C_t) \times V}{m} \qquad (3)$$

$$D = \frac{K\lambda}{\beta \cos\theta} \qquad (4)$$

where, C_0 and C_t are the concentration of contaminant at initial ($t = 0$) and time t (min), respectively; k is the pseudo first-order rate constant (the k value was calculated from the slope of the ln (C_0/C_t) − t plots); V is the volume of solution (L) and m is the mass of the catalyst (g).

2.6 Antibacterial Study

In this study, the antibacterial ability of the as-prepared nanomaterials was evaluated by agar plate diffusion method. *Escherichia coli* (ATCC 25922), a gram-negative bacterial strain, was chosen as the model organism in order to perform antibacterial activities of the as-synthesized products. The *E. coli* bacteria was cultivated in sterilized Luria–Bertani Broth at 37 °C with continuous shaking at 150 rpm for 6 h under aerobic condition. Then, the grown broth culture was adjusted to ($10^6 \div 10^8$) CFU/mL as standard and swabbed uniformly across an agar plate. The as-synthesized ZnO and heterostructure Au/ZnO composites were diluted with NaCl 0.85% solution to form a suspension with obtained different concentrations

of 50, 100, and 200 mg/mL. Afterward, sterile standard cellulose filter papers with a diameter of 6 mm impregnated test samples were placed on the surface of the agar, while the filter papers without the dispersion of materials were used as a negative control. Finally, the prepared plates were incubated in the incubator at 37 °C for 24 h. The disk constituents diffuse from the filter paper into the agar and inhibit the growth of bacteria. Thus, after the incubation, the inhibition zones around the wells were observed.

3. Results and Discussion

3.1 Physiochemical Characterization

The SEM results are indicated in Figure 2. The pure ZnO sample was seen as a uniformly stratified structure like rose flowers. Microstructures about 10 micrometers in size are made up of many thin sheets showing a thickness of 10÷20 nm (Figure 1(a-b)). After doping Au into the composite, the stratified structure of ZnO was not changed, it can be seen that Au NPs were dispersed on the microstructure ZnO in all of the doped samples, however, their dispersions were different according to each method. The Au particles were evenly dispersed on ZnO in Au/ZnO-SC composite (Figure 2(d-f)). This was similarly observed for the Au/ZnO-SB
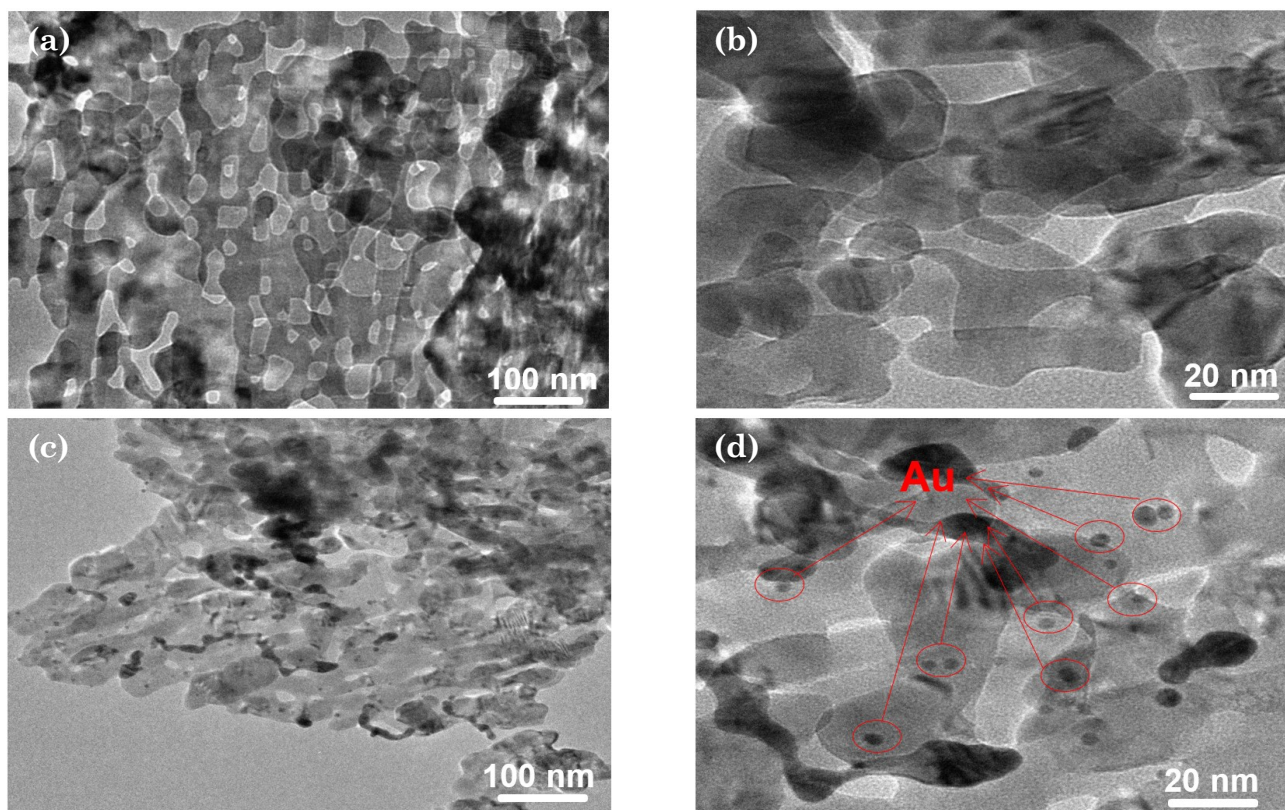

Figure 3. TEM images of (a-b) as-synthesized ZnO and (c-d) Au/ZnO-SC samples with different bars.

sample, in Figure 2 (g-i). Both of these samples were porous, the petals were uniformly arranged, and it could be observed that Au NPs with small sizes were anchored on the surfaces of the petals. However, the reduction process resulted in a part of both samples being broken. Unlike Au/ZnO-SC and Au/ZnO-SB composites, Au NPs were very densely distributed on the surface of Au/ZnO-SE and Au/ZnO-Hg lamp samples. The ZnO microstructure was shrunk and separated from each other, in Figure 2(k-m). The Au/ZnO-Hg lamp sample showed tighter and denser after loading the gold than other composites as shown in Figure 2(n-p). The temperature of the reduction process and the rapid reaction rate of sodium citrate and sodium borohydride with $HAuCl_4$ might be the reasons for the difference in the dispersion of Au NPs. The rate of Au nanoparticle generation at room temperature could lead to uniformly dispersing and keeping the original structure of ZnO after the reaction.

The TEM results of ZnO and Au/ZnO-SC in various scale bars are presented in Figure 3. Clearly, it revealed that many pore structures in the size range of 20÷50 nm were formed on the ZnO surface, which was an important contributor to photocatalytic processes Figure 3(a-b). By virtue of these pore structures, ZnO nanoparticles (ZnO NPs) have the significant abil-

ity to diffuse light as well as efficiently transport hydroxyl radicals in photochemical reactions, leading to enhancing their photocatalytic performance of them [31,33]. By comparison, after doping Au NPs into ZnO, the holes tended to be narrower on the petals, it was not as smooth as that of the original ZnO. Figure 3(c-d) showed the uniformly dispersed Au NPs with particle sizes of approximately 2÷5 nm on the surface of ZnO.

The crystal wurtzite ZnO phase was revealed by XRD pattern in Figure 4(a), which showed the (100), (002), (101), (102), (110), (103), (112), and (201) planes at 2θ of 31.7, 34.4, 36.2, 47.5, 56.6, 62.8, and 67.9°, respectively (JCPDS card No. 36-1451) [31]. In addition, the other diffraction peaks at 38.2, 44.4, and 64.5° were specified to the (111), (200), and (220) crystal planes of crystal Au particles [34], in the Au/ZnO-Hg lamp sample. However, the intensity of these peaks was gradually reduced for Au/ZnO-SE and Au/ZnO-SB samples, these peaks almost disappeared for Au/ZnO-SC. The content of Au was low and the size of Au nanoparticles was infinitesimal, which were causes of the XRD signal coverage of Au by ZnO [35]. Besides, no shift and impurities diffraction peaks were observed.

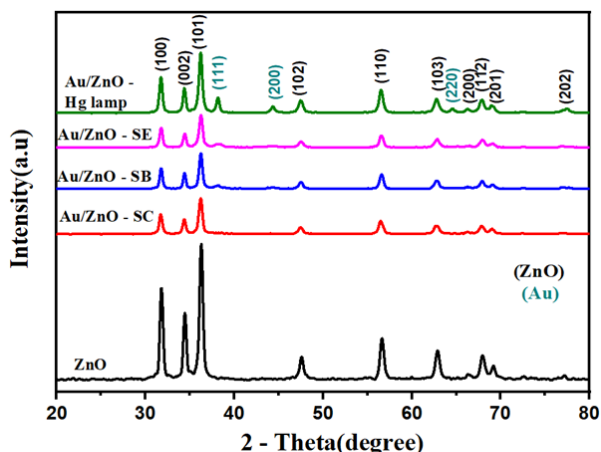The crystal sizes of as-prepared samples were determined through Debye–Scherrer

Figure 4. XRD patterns of as-synthesized Au/ZnO-SC, Au/ZnO-SB, Au/ZnO-SE and Au/ZnO-Hg lamp samples.
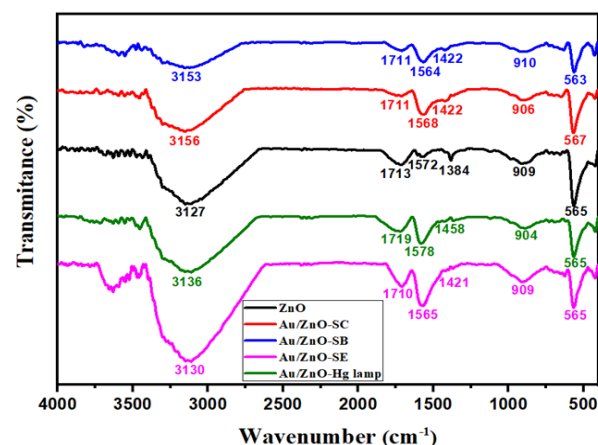

Figure 5. IR spectrums of as-synthesized Au/ZnO-SC, Au/ZnO-SB, Au/ZnO-SE and Au/ZnO-Hg lamp samples.

Table 1. Textural properties of as-prepared ZnO and Au/ZnO samples.

Sample	E_g (eV)	Average crystallite size D (nm)	S_{BET} (m²/g)	BJH pore volume (cm³/g)	Average pore width (nm)
ZnO	3.202	18.02	24.40	0.408	47.9
Au/ZnO-SC	3.164	15.54	26.23	0.263	33.2
Au/ZnO-SB	3.139	17.19	26.22	0.255	32.8
Au/ZnO-SE	3.157	15.78	24.53	0.241	32.9
Au/ZnO-Lamp Hg	3.174	16.16	23.22	0.220	32.7

equation [32]:

$$D = \frac{K\lambda}{\beta \cos\theta} \qquad (4)$$

where, $K = 0.9$, $\lambda = 1.54$ (the wavelength of X-ray), β is the full width at half maximum in radians (FWHM) and θ is the Bragg's diffraction angle. As shown in Table 1, the average size of ZnO is slightly larger than that of the composites, which can be indicated by the distortion

in the host ZnO lattice by the external impurity Au, and the degree of influence depends on the different doping methods [36].

The composition, structure, and function groups of samples were demonstrated by FT-IR [37]. The FT-IR spectra of as-synthesized ZnO were almost non-different from that of Au/ZnO composites, as shown in Figure 5. The broad and strong bands from about 3100 to 3200 cm⁻¹ corresponded to the O−H stretching vibration
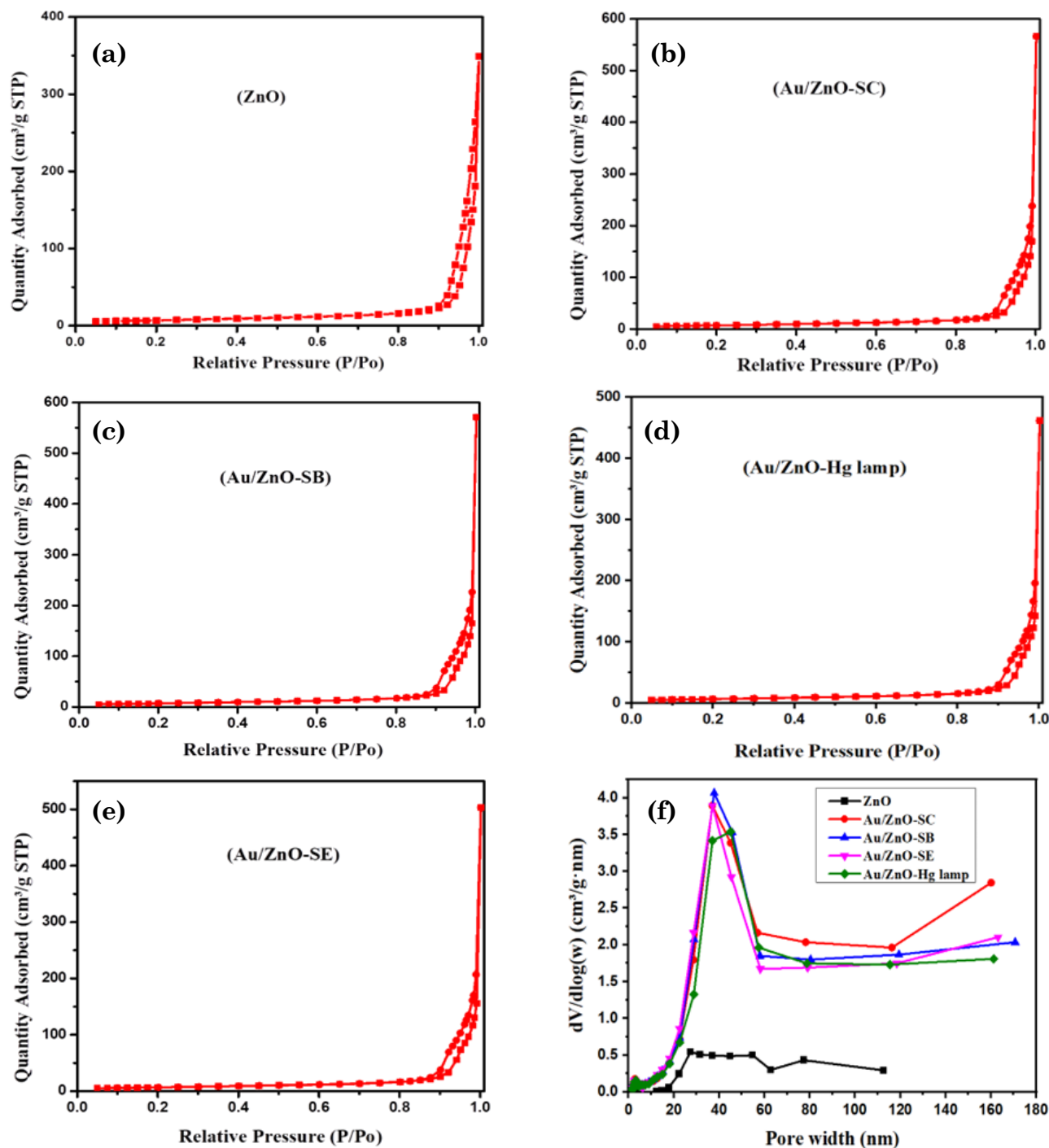

Figure 6. (a), (b), (c) and (d) N$_2$ adsorption/desorption isotherms of Au/ZnO-SC, Au/ZnO-SB, Au/ZnO-SE and Au/ZnO-Hg lamp, respectively, and (e) pore size distributions.

in water molecules absorbed on the surface [38]. The peaks at 1572, 1568, 1564, 1565, and 1578 cm^{-1} in all the FT-IR spectrums could be indexed to the C=O bond in −COOH groups [39]. Meanwhile, the small band of about 1713, 1420, and 906 cm^{-1} were ascribed to the vibration of the O−H bond in zinc hydroxide [40]. In particular, the intense bands at more or less 565 cm^{-1} confirmed the stretching vibration of Zn−O bonds in ZnO and composites [41].

Figure 6 illustrates the N$_2$ isotherms of as-prepared samples. According to IUPAC, the adsorption isotherms of all samples were classified as type IV with H3 hysteresis loops, which are characteristic of mesoporous material [42]. It can be seen that the hysteresis loops appeared evidently in the P/P0 range of 0.91 0.98. Notwithstanding, the hysteresis loops of composites were similar to that of ZnO, and the nitrogen adsorption abruptly grew at P/P0 higher than 0.98.

The pore size of ZnO was distributed in the range from 20 to about 120 nm with a major pore size of 28 nm. Meanwhile, after doping Au, the pore size distribution of as-synthesized composites experienced significant variations. The pore size of Au/ZnO samples was distributed larger than pure ZnO and fluctuated from about 5 to approximately 160 nm. Whereas the intensity of pores of Au/ZnO-SC, Au/ZnO-SB, and Au/ZnO-SE samples was most popular at around 35 nm, that of the Au/ZnO-Hg lamp reached a peak of 40 nm. The increase in pore size intensity of Au-doped composites compared with pure ZnO can be explained by the agglomeration of the ZnO structure occurring through the reduction of gold salts.

The BET surface areas of all doped samples were slightly larger than ZnO, except Au/ZnO-Hg lamp, in Table 1. By contrast, Barrett-Joyner-Halenda (BJH) pore volume and average pore width of as-synthesized composites
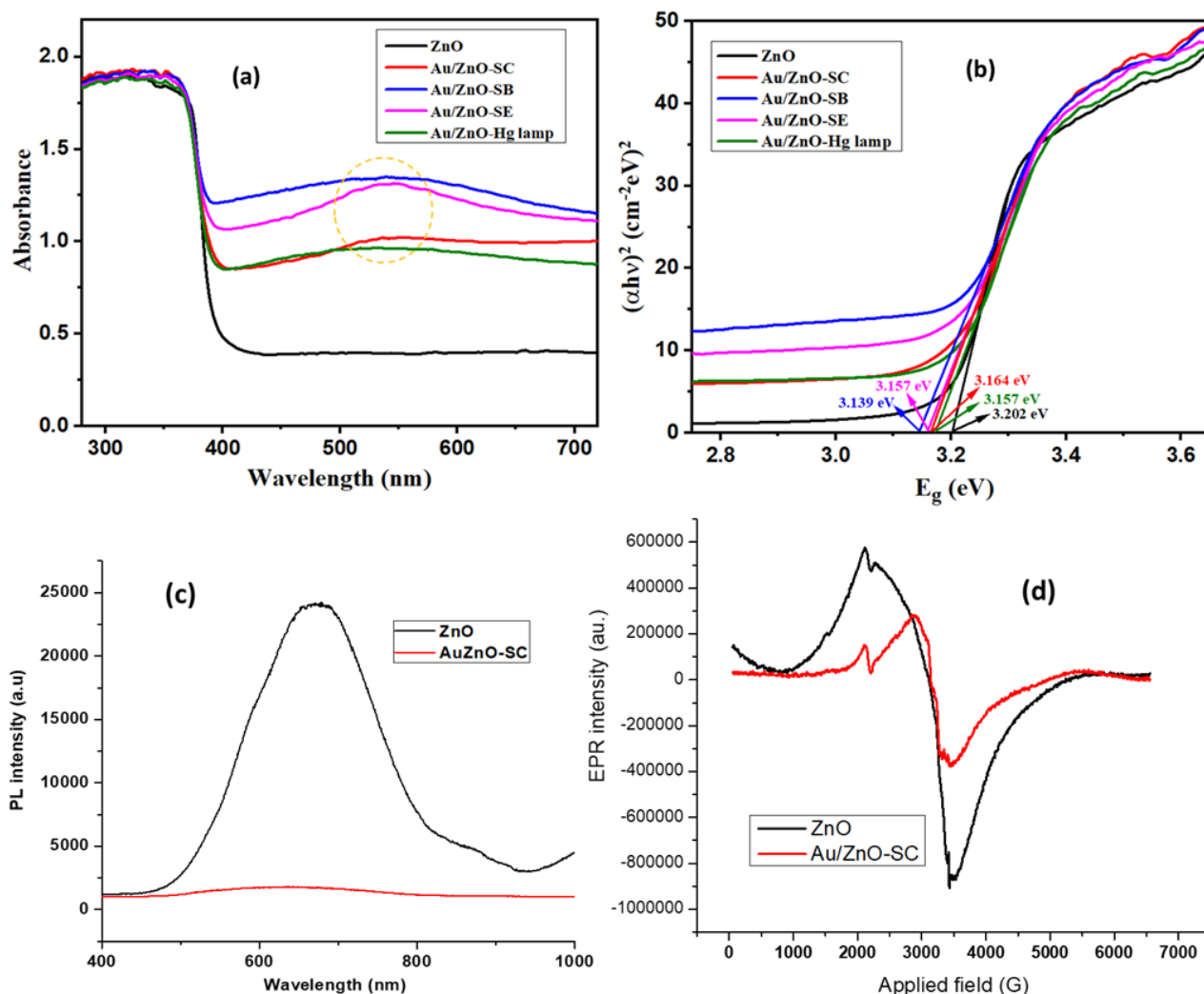

Figure 7. (a) UV-Vis diffuse reflectance spectra, (b) Tauc's plot of the as-synthesized ZnO, Au/ZnO-SC, Au/ZnO-SB, Au/ZnO-SE and Au/ZnO-Hg lamp samples, (c) and (d) PL spectra and EPR spectra of ZnO and Au/ZnO-SC.

were lower than those of ZnO, 0.408 cm³/g and 47.9 nm, respectively. Meanwhile, the BJH pore volume of ZnO samples decorated with Au NPs was in the range of 0.220÷0.263 cm³/g and the average pore width of them had values between 32 and 34 nm. Amongst as-prepared composites, Au/ZnO-SC had the largest surface area and the highest pore volume and average pore width, these can be expected to give the good photocatalytic ability to degrade toxic organic pollutants of composites.

The optical properties of the materials have a great influence on the catalytic activity, which in many studies can be analyzed by absorption spectroscopy [43]. In general, all samples strongly absorbed UV light in the 250÷350 nm region, followed by an absorption edge at 375 nm, which is attributed to the interband excitation in the ZnO NPs [44]. However, composites had stronger near ultraviolet region of 350÷400 nm adsorption than pure ZnO. Additionally, it is seen from Figure 7(a) that the appearance of absorption peaks represented by a dashed circle in the visible light region (500÷600 nm) was due to the SPR effect of Au NPs [45]. The shape and position of the precious metal SPR bands depend on various parameters such as the shape and size of the nanoparticles, the dielectric constant as well as environmental factors [37].

Besides, the absorption peaks position shift as decorating Au NPs on the surface of ZnO also could be able to lead to the change in the bandgap energy, which was calculated through Tauc's equation [34]:

$$(\alpha h\upsilon)^{1/n} = A\left(h\upsilon - E_g\right) \quad (5)$$

where, α is the absorption coefficient, h is the Planck constant, υ is the photon's frequency, A is a constant, E_g is the average band gap energy of material and n has the value depending on the type of transition. Since ZnO exhibits direct optical transition, the value of n is 1/2 in this study. The optical band gap is determined by extrapolation of the linear portion in the plot of $(\alpha h\upsilon)^2$ against $h\upsilon$ as shown in Figure 7(b) and the results are presented in Table 1. The band gap energy of ZnO of 3.202 eV is higher than Au/ZnO-SC, Au/ZnO-SB, Au/ZnO-SE, and Au/ZnO-Hg lamp samples with the values of 3.164, 3.139, 3.157 and 3.174 eV, respectively. This proves that the addition of Au NPs into the ZnO surface led to the reduction in the band gap energy of Au/ZnO samples compared to pure ZnO, resulting in enhancing their photocatalytic performance under visible light irradiation. The reduction of the optical band gap can be related to the higher light absorption intensity of Au NPs in the visible region by virtue of their plasmon resonance ability. It is predicted that the increase in absorption intensity can enhance the photocatalytic efficiency under visible light irradiation, especially solar light, of Au/ZnO catalysts after the decoration of Au NPs on ZnO [46].

The PL spectra of the ZnO and Au/ZnO-SC samples are shown in Figure 7(c). The PL spectrum of ZnO exhibited a broad band with a peak of 665 nm, which was a red mission arising from structural defects or the recombination of photogenerated carriers with single ionic charge states [47]. Meanwhile, the Au/ZnO-SC sample exhibits low emission revealing the reduction of the recombination of electrons and holes. These were expected to give an enhanced photocatalytic to the Au/ZnO composites.

Electron magnetic resonance (EPR) is a highly sensitive analytical technique for the detection of unpaired electrons and oxygen vacancies of Vo (+2 charge state), Vo• (+1 charge state) and Vo•• (0 charge state. Vo was rarely detected in n-type ZnO, while Vo•• was easy to generate because of its low formation energy [48]. As shown in Figure 7(d), the signal at g = 1.965 on both ZnO and Au/ZnO-SC samples was attributed to oxygen vacancy Vo• [49], but the presence of Au led to a decrease in signal strength of Au/ZnO-SC composite. This could be explained that the electrons of Au nanoparticles were transferred to ZnO and then paired with the lone electrons in Vo•, leading to the formation of paramagnetic Vo••. Which was the reason for the decrease in the recombination of electrons and holes. It was expected an increase in the photocatalytic ability of Au/ZnO composite.

3.2 Examination of Photocatalysis

3.2.1 Degradation of tartrazine on ZnO and Au/ZnO

The experiments were carried out at 0.05 g catalyst, 10 mg/L TA, Hg lamp 250 W. As the results are demonstrated in Figure 8, the degradation performance of TA was affected by different methods of Au/ZnO synthesis. The Au/ZnO-SC, Au/ZnO-SB, and Au/ZnO-SE samples had higher photodegradation efficiency and the reaction than pure ZnO, while Au/ZnO-Hg lamp experienced the opposite pattern. Pure ZnO had a DE of 78% and a rate constant of 0.031 min⁻¹. The Au/ZnO-SC completely degraded TA within 30 min with a rate constant of 0.124 min⁻¹, and the Au/ZnO-SB sample completely degraded TA within 40 min with a

rate constant of 0.117 min^{-1}. The DE and rate constant for Au/ZnO-SE within 50 min were 85% and 0.039 min^{-1}, respectively. Meanwhile, the Au/ZnO-Hg lamp only showed 63% and 0.018 min^{-1}, respectively. These results demonstrate that doping Au NPs on the surface of flower-ZnO can improve TA degradation in terms of both yield and reaction rate compared with pure ZnO, with the exception of Au/ZnO-Hg. In addition, the degradation capacity during 30 min of Au/ZnO-SC reached the value of about 20 mg/g higher than the remaining samples as shown in Figure 8(c). The Au/ZnO-SC nanocomposite was the most effective catalyst of four as-synthesized Au/ZnO samples, which was due to the combination of factors such as the uniform dispersion of Au NPs on the surface as well as surrounding petals of flower-like ZnO structure with a small Au particle size, the reduced band gap energy compared to ZnO, and the large BET surface area.

3.2.2 Examination with the initial pH value of TA solution

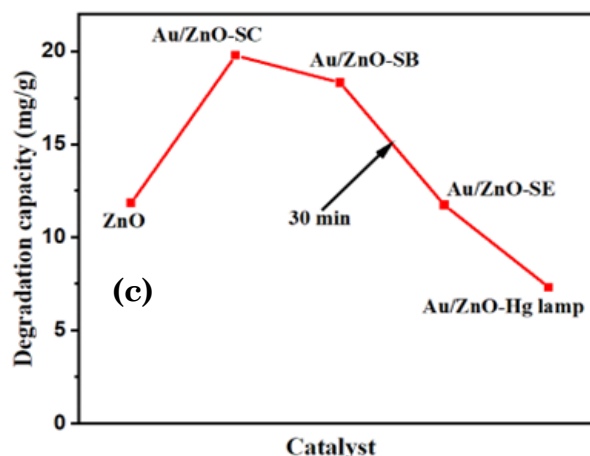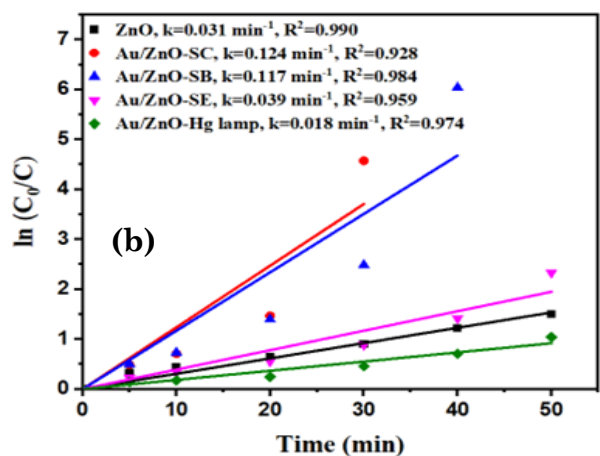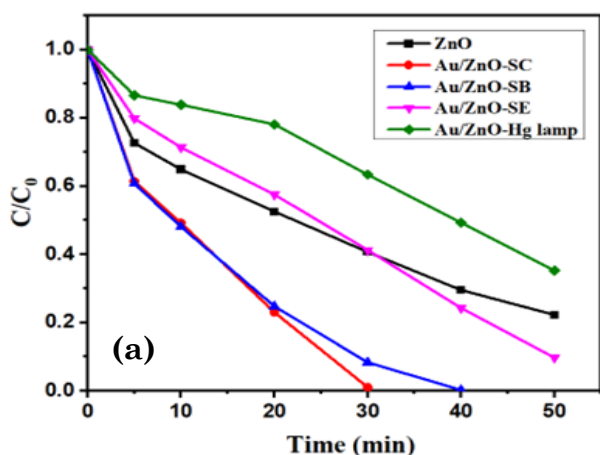pH is a crucial factor affecting the treatment of toxic organic contaminants in

Figure 8. (a) Effect of as-synthesized ZnO, Au/ZnO-SC, Au/ZnO-SB, Au/ZnO-SE and Au/ZnO-Hg lamp samples on photodegradation of tartrazine and (b) first-order curves. The reaction conditions: catalyst dosage of 0.5 g/L, TA concentration of 10 mg/L, and Hg lamp 250 W.
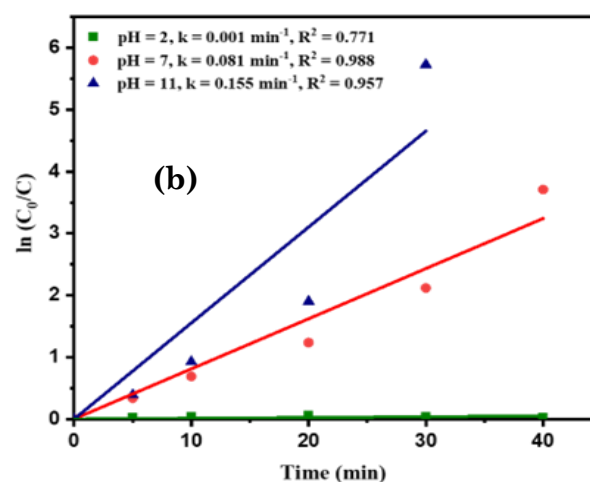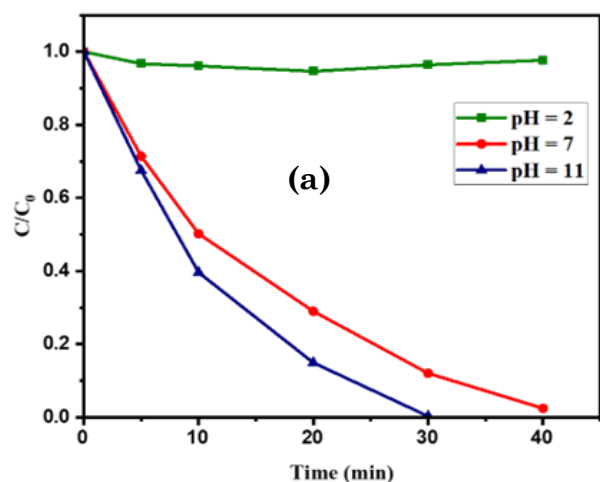

Figure 9. (a) Effect of initial pH on photodegradation of TA and (b) first-order curves. The reaction conditions: catalyst dosage of 0.5 g/L, TA concentration of 10 mg/L, and Hg lamp 250 W.

wastewater by photocatalysts. In this study, the efficiency of the process at acidic, neutral, and alkaline conditions was also investigated and evaluated. pH of the initial TA solution was adjusted to pH values of 2, 7, and 11 by HCl 0.1 M and NaOH 0.1 M solutions before investigating its degradation by the Au/ZnO-SC catalyst under the same reaction conditions: catalyst dosage of 0.5 g/L, TA concentration of 10 mg/L, and Hg lamp 250 W irradiation. As the results shown in Figure 9, the photodegradation efficiency of TA in Au/ZnO-SC composite was extremely low, exhibiting a DE of approximately 3% and with the reaction rate of 0.001 min^{-1}. Since ZnO could be protonated in the acidic environment to generate Zn^{2+} (ZnO (s) + $2H^+$ (aq) $\rightarrow$ Zn^{2+} (aq) + H_2O), it was no longer photocatalytic activity, causing the significant decrease in TA degradation. On the contrary, in the alkaline medium, on the surface of the catalyst as well as in the reaction solution appeared large amounts of OH^- ions, and through photocatalysis, they formed OH radicals, which is a strong oxidizing agent and much more likely to attack and decompose the organic pollutants in waste water. Consequently, at pH =

11, the photocatalytic performance of Au/ZnO-SC composite was considerably enhanced with the DE and the rate constant of 100% and 0.155 min^{-1}, respectively. Notwithstanding, if waste water adjusted to a high pH value, it must be neutralized before being released into the environment.

As initial pH value of TA solution was adjusted to neutral media, the photocatalytic activity of Au/ZnO-SC composite was relatively good and decomposed 97.5% TA within 40 min with the reaction rate of 0.081 min^{-1} as shown in Figure 9. It can be explained that due to the effective adsorption of organics on the surface of the material at pH = 7, which depends on the pH point of zero charge (pHPZC). The pHPZC of Au/ZnO composite was investigated by the pH drift method in our previous report and reached a value of 7.4 [50]. Hence, at pH = 7, below pHPZC of catalyst, H^+ ions adsorbed on the surface of the Au/ZnO-SC sample. As a consequence, the photocatalyst's surface was positively charged, leading to effective adsorption of TA anions, enhancing substantially the dye degradation performance.
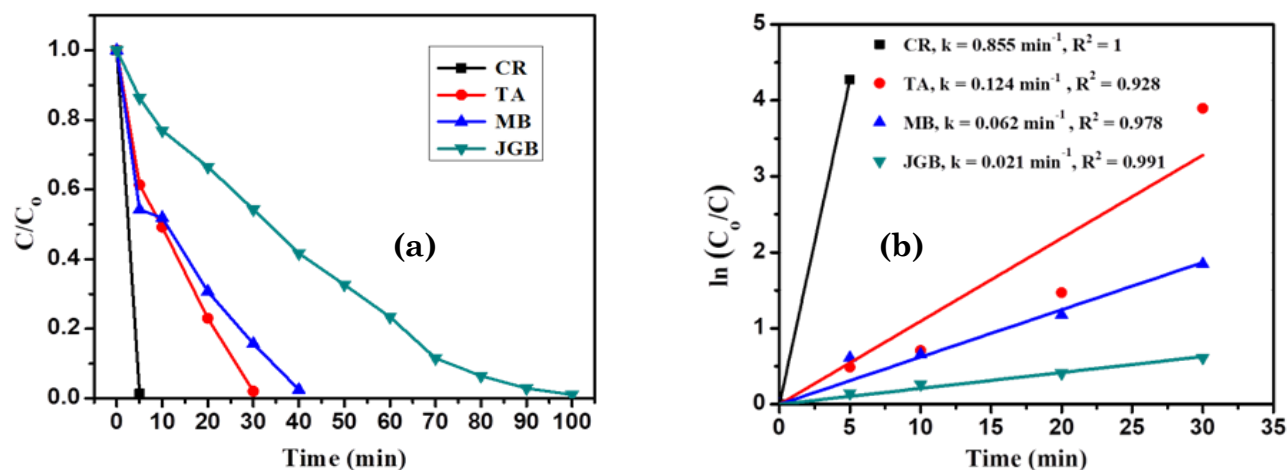
Figure 10. (a) Degradation of some organic dyes under Hg lamp 250W on Au/ZnO-SC: [catalyst] = 0.5 g/L, [initial organic dyes concentration] = 10 mg/L and (b) the kinetic curves.

Table 2. Comparison of photocatalytic degradation of different organic dyes using ZnO-based nanocomposites.

Catalyst, Dosage (g/L)	Target pollutant (concentration, mg/L)	Light source	Degradation time/efficiency	Reference
CuO/ZnO, 1 g/L	CR (50 mg/L)	Xe lamp 350 W	50 min/91 %	[56]
Au/ZnO-SC, 0.5 g/L	CR (10 mg/L)	Hg lamp 250 W	5 min/100 %	This work
Ni/ZnO, 5 g/L	MB (20 mg/L)	UV lamp 80 W	18 h/93 %	[57]
Au/ZnO-SC, 0.5 g/L	MB (10 mg/L)	Hg lamp 250 W	40 min/98.7 %	This work
Ag/ZnO, 0.5 g/L	JGB (10mg/L)	Solar light	60 min/83 %	[31]
Au/ZnO-SC, 0.5 g/L	JGB (10 mg/L)	Hg lamp 250 W	100 min/99.5 %	This work
(Ce, Ag) co-doped ZnO, 1.0 g/L	TA (10 mg/L)	UV lamp 24 W	90 min/98.91 %	[58]
Au/ZnO-SC, 0.5 g/L	TA (10 mg/L)	Hg lamp 250 W	30 min/100 %	This work

3.2.3 Examination with the different organic dyes

The photocatalytic activity of a material depends not only on its physical and chemical properties but also on the properties of organic contaminants. Therefore, besides studying the photocatalytic degradation of TA the performance of the Au/ZnO-SC sample was also evaluated by other prevalent organic compounds such as CR, JGB, and MB under the optimal conditions. As seen in Figure 10, Au/ZnO can almost completely remove CR, TA, JGB, and MB after 10, 30, 40, and 100 min of reaction, respectively. For instance, CR was found to be the highest reaction rate of 0.855 min^{-1}, followed by TA and MB with a reaction rate of 0.124 min^{-1} and 0.062 min^{-1}, respectively. Meanwhile, the reaction rate of JGB was lowest among tested dyes, it was 0.021 min^{-1}.

Table 2 shows a brief comparison of the photocatalytic efficiency of ZnO-based nanocomposites in removing persistent organic compounds in wastewater. It can be clearly observed that the degradation efficiency of Au/ZnO-SC material in this study was much more than that of other ZnO-based catalysts. From these results, Au/ZnO material can be used as a potential photocatalyst in wastewater treatment.

3.2.4 Reusability of catalyst

The reuse of photocatalysts is crucial to their practical application because it is related to the efficiency and cost of the entire process. The reusability of the Au/ZnO-SC material was evaluated by its photocatalytic performance over three consecutive cycles. After each experiment, the powder catalyst was collected by vacuum pump filtration, washed several times with distilled water and ethanol, dried in air at 80 °C for 12 h, and reused for subsequent experiments. The degradation efficiency of TA under Hg lamp 250 W revealed a drop to 76% after three recycling tests, in Figure 11(a). The decrease in catalytic efficiency could be due to the loss of active sites or due to a change in the structure of the material, the particle size became smaller and the crystallinity was reduced after the catalysis process. This demonstrated that the intensity of the XRD peaks of the sample after 3 three recycling experiments was reduced compared with that of the unused sample, shown in Figure 11(b).

3.2.5 The photocatalytic mechanism

Figure 12 illustrates the reaction mechanism of TA on Au/ZnO composite. As ZnO is irradiated by a light source with the photonic energy ($h\upsilon$) greater than or equal to its band gap energy (E_g), the electrons in the valence band (VB) can be excited (e$^-$) and transfer to the conduct band (CB), leading to holes (h$^+$) generation in the VB. The electron-hole pairs react with oxygen or H$_2$O adsorbed on the surface of the material to produce reactive oxygen species
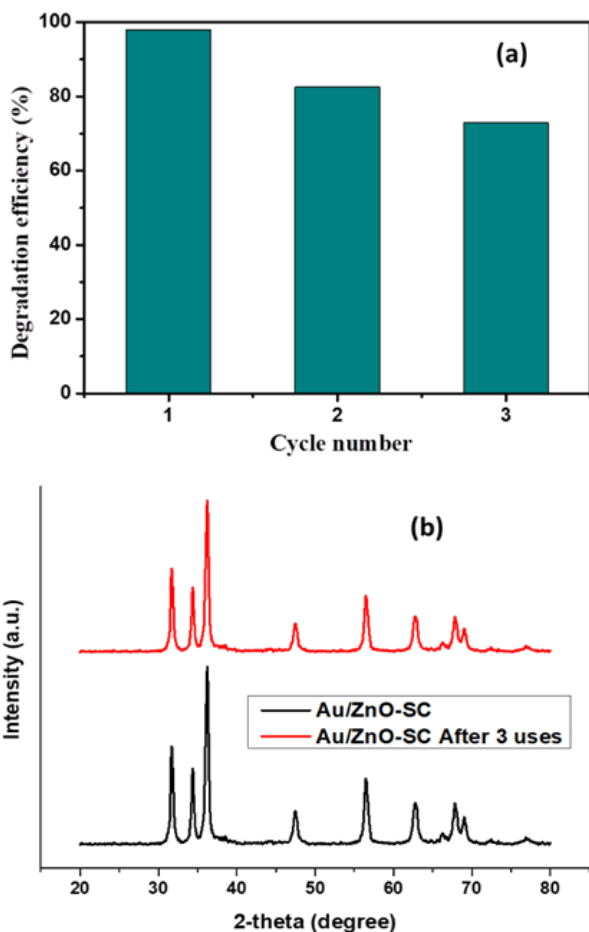

Figure 11. (a) Reusability test of as-synthesized Au/ZnO-SC sample, (b) XRD pattern of Au/ZnO-SC after 3 uses.
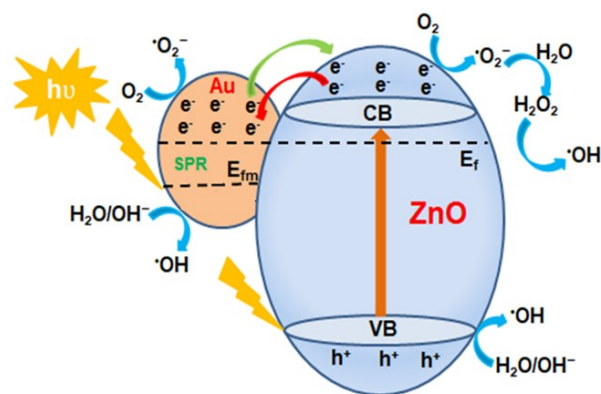

Figure 12. Schematic model for the photocatalytic mechanism of Au/ZnO nanocomposite.

(ROS) such as superoxide anion radicals $\cdot O_2$, hydroxyl radicals ($\cdot OH$), and hydrogen peroxide (H_2O_2). ROS are considered, powerful oxidizing agents, therefore, they will quickly attack the organic pollutant molecules to form intermediate compounds, eventually produce to carbon dioxide and water ideally. The presented degradation mechanism was suggested in our previous study [50]. However, as aforementioned information, the limitation of the ZnO is the rapid recombination rate between electrons and holes. After an extremely short time, electrons tend to release energy instantaneously to return to the ground state and recombine with holes. In addition to this, owing to the high band gap energy, ZnO exhibits low absorption efficiency in the visible light region. These disadvantages have restricted the practical applications of ZnO.

When Au nanoparticles are added to the surface of ZnO, the establishment of the Schottky barrier at the interface between Au and ZnO helps electrons in CB of ZnO transfer easily to Au [51], as illustrated by the red arrow in Figure 12. Consequently, Au NPs act as electron traps from the semiconductor, taking responsibility for prolonging the lifetime of the charge carriers on the surface of ZnO as well as inhibiting their recombination of them [52].

On the other hand, as illuminated with a visible light source, the electrons are formed in the metallic Au NPs via SPR, as a result, Au/ZnO nanocomposite is more likely to absorb strong light irradiation in the visible region. As Fermi energy is stimulated to the SPR state, the electrons on the surface of Au migrate into the CB of ZnO as described by the green arrow in Figure 12, followed by the participation in the photocatalytic process.

Based on the above analysis, it is apparent that the combination between the Au NPs and the ZnO semiconductor can be able to not only boost its light absorption capacity in visible irradiation but also enhance the separation efficiency of photogenerated electron–hole pairs. Thus, Au/ZnO nanocomposites possess good photocatalytic activity and high stability, which clarified the availability of Au/ZnO in the photocatalysis field synthesized in our experiments.

3.3 Antibacterial Activity of As-Synthesized Samples

3.3.1 Antibacterial activity against E. coli

The inhibition zones on the surface of agar plates demonstrated the antibacterial ability of as-prepared samples. The larger the diameter of the antibacterial ring, the higher the antimicrobial activity of the test material. As the results demonstrated in Figure 13, the inhibition zones of the negative control samples on the agar plates almost did not appear, which proves E.coli bacteria still grew well under the research conditions. Meanwhile, in the presence of as-synthesized samples, antibacterial
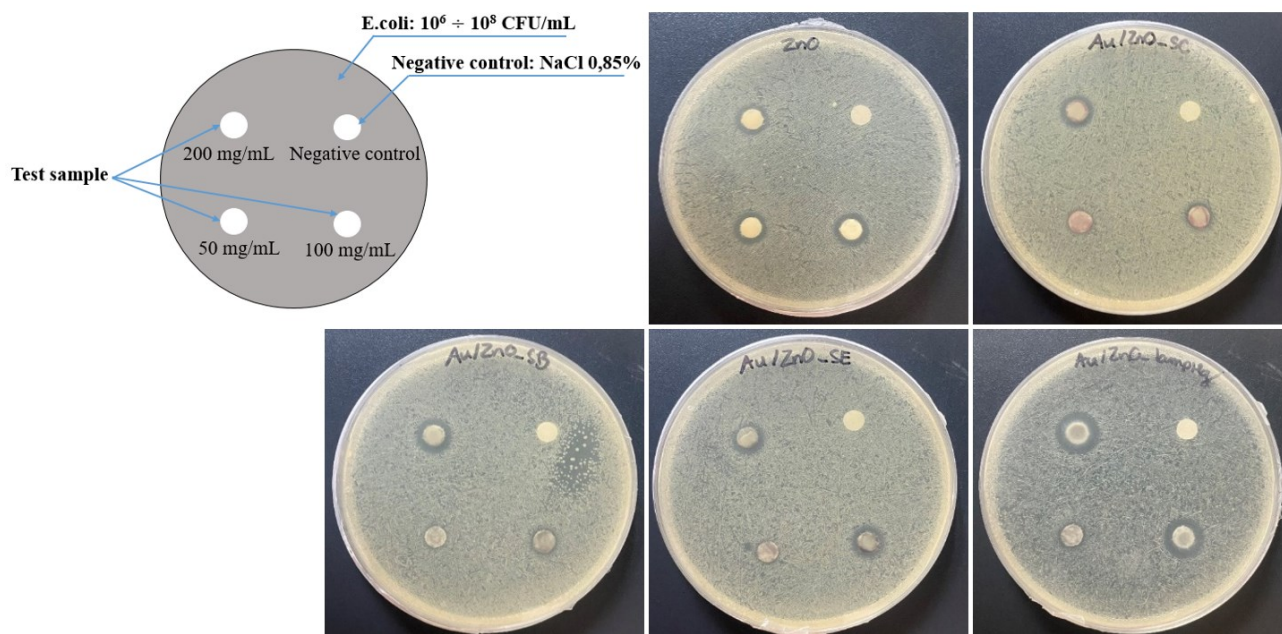

Figure 13. The results of agar plate diffusion test to evaluate the antibacterial activity of as-synthesized ZnO, Au/ZnO-SC, Au/ZnO-SB, Au/ZnO-SE and Au/ZnO-Hg lamp (negative control, 50 mg/mL, 100 mg/mL and 200 mg/mL samples arranged in the order shown in the illustration).

rings are clearly observed. Pure ZnO showed pretty good antibacterial activity against *E. coli*. After doping Au NPs, the obtained samples had different antibacterial activities depending on the synthesis methods. Which,
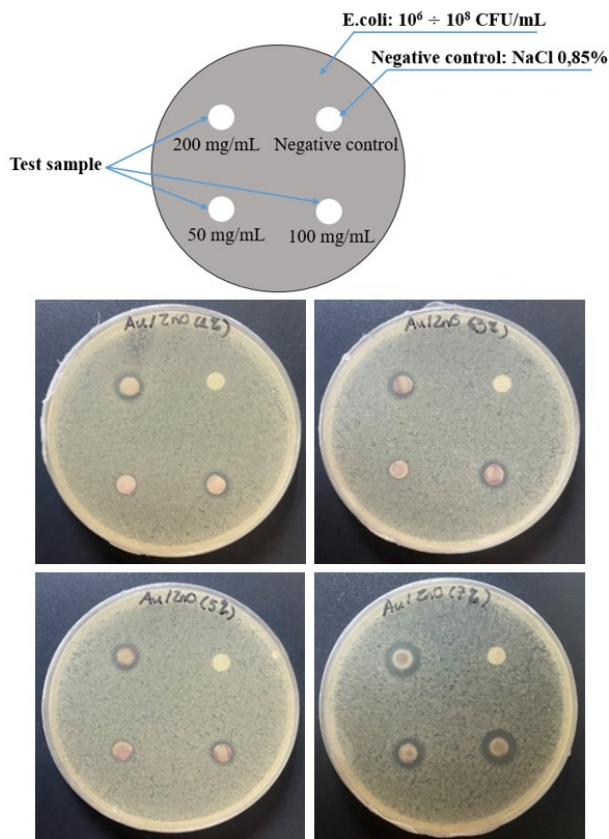

Figure 14. Effect of Au content doped on ZnO (1, 3, 5, and 7 wt.% of Au) on antibacterial activity of Au/ZnO-SC (negative control, 50 mg/mL, 100 mg/mL and 200 mg/mL samples arranged in the order shown in the illustration).

Au/ZnO-Hg lamp shows the best antibacterial activity compared to the remaining samples since the diameter of antibacterial rings of Au/ZnO-lamp Hg is significantly larger than those of pure ZnO and other Au/ZnO products.

The bacterial inhibition zone is also affected by the amount of antibacterial agent. Overall, the higher the concentration of ZnO and Au/ZnO samples used, the better they had the ability to kill *E. coli*. All the as-prepared samples at the concentration of 200 mg/mL exhibited antibacterial activity against *E. coli* more effectively than at that of 50 mg/mL and 100 mg/mL, as shown in Figure 13. Moreover, a remarkable antibacterial efficiency was also recorded while the survival of *E. coli* decreased further as the contents of Au doping on the ZnO matrix increased. In Figure 14, as the concentration of Au content increased from 1 to 7 wt%, the efficiency in killing *E. coli* of Au/ZnO-SC increased clearly. Especially, Au/ZnO-SC at 7 wt% showed a significantly enhanced inhibition zone with all concentrations of antibacterial agent used at 50, 100, and 200 mg/mL.

3.3.2 The antibacterial mechanisms

Up to now, the exact mechanism of antibacterial activity of both ZnO and Au/ZnO is still vague. Based on some previous research reports, this mechanism is identified through three main pathways: generation of ROS, the release of Zn^{2+} and Au^+ ions, and attachment of nanoparticles to the bacteria cell membrane [23,24,53]. A schematic illustrating all the possible probable pathways using as-prepared Au/ZnO nanocomposite to be fatal for *E. coli* has been shown in Figure 15.
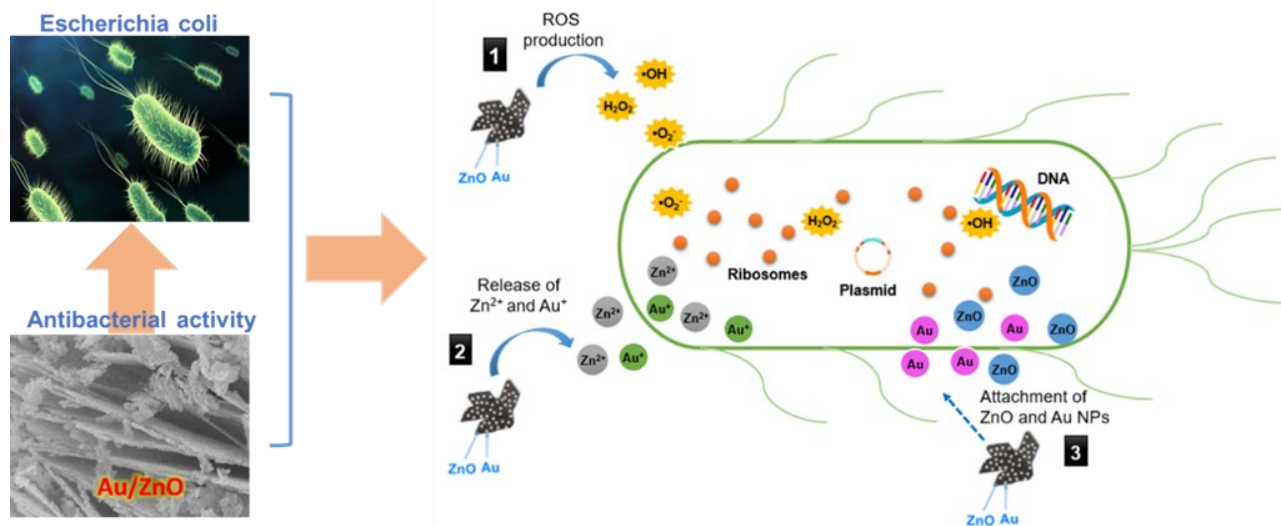

Figure 15. Mechanism of antibacterial activity against *E. coli* of Au/ZnO composite.

(1) Generation of ROS: According to the photocatalytic mechanism of ZnO and Au/ZnO presented above, under light radiation with proper energy, these nanoparticles generate photoexcited electrons and holes, which interact with O_2 or H_2O absorbed on the surface of catalysts to produce ROS such as superoxide anion ($\cdot O_2^-$), hydroxyl radicals ($\cdot OH$) and hydrogen peroxide (H_2O_2). Amongst them, $\cdot OH$ is the most reactive oxygen species, therefore, it attacks quickly organic biomolecules, including nucleic acids, lipids, carbohydrates, proteins, and DNA [23]. Similarly, H_2O_2 also penetrates the bacterial membrane and disrupts the internal components of the cell. Whereas, $\cdot O_2^-$ is not likely to enter the membrane because of its negative charge, hence, it only can be observed on the outer surface as in Figure 15 [24]. Eventually, these ROS induce cell membrane oxidation and degradation causing injuries and bacterial cell death.

(2) Release of Zn^{2+} and Au^+: The release of Zn^{2+} and Au^+ ions in an aqueous solution plays an important role in the antibacterial mechanisms of ZnO and Au/ZnO. The Zn^{2+} and Au^+ ions can easily enter the cells membrane by virtue of the interaction between them and bacterial cells. Subsequently, these ions directly interact with the functional groups on bioactive proteases, such as sulfhydryl, amino, and hydroxyl groups, resulting in the inhibition of bacterial cell activities including metabolism and enzyme activity [54]. Thus, they rapidly disrupt the cellular integrity and induced the cell to die.

(3) The direct attachment of ZnO and Au nanoparticles to the bacteria cell membrane via electrostatic forces: The positively charged Au and ZnO nanoparticles will be electrostatically attracted to the negatively charged bacterial cell, they can penetrate the cell membrane [55]. This interaction may disturb the charge balance of the cell surface, and damage the membrane plasma structure, leading to the leakage of intracellular components. In addition, the accumulation of nanoparticles in the cell also interfered with the metabolic functions of the bacteria [24]. Therefore, bacteria are easily destroyed.

In this study, breakage of the cell membrane was predicted mainly through direct interaction between Zn^{2+} and Au^+ ions as well as ZnO and Au nanoparticles and bacterial cells, that not due to ROS formation. Hence, when Au nanoparticles decorated on the surface of ZnO have a large size, they are favorable for interaction with the cell membrane. At the same time, with a large concentration of Au doped on ZnO, more Au^+ ions will be released, and the number of Au nanoparticles directly attacking the cell membrane will increase, thereby increasing the efficiency in killing *E. coli*. As a result, coating Au NPs on ZnO enhances the antimicrobial performance of ZnO.

4. Conclusion

ZnO was prepared by hydrothermal method to obtain a hierarchical structure like a flower with crystallites of hexagonal wurtzite type. Au nanoparticles were successfully doped into the surface of ZnO using different Au^{3+} reducing agents. It has been found that the combination of Au nanoparticles with ZnO photocatalyst could open avenues to develop tunable photocatalysts whose reactivity can be controlled by the size, shape, and loading of gold nanoparticles, which is strongly influenced by the synthesis methods. As a result, Au/ZnO-SC achieved the highest photocatalytic efficiency compared with doped samples for removal of toxic organic contaminants under visible light irradiation, especially TA and CR, thanks to high purity, uniformly distributed Au nanoparticles, larger BET surface area and pore volume and a decrease of band gap energy. The enhanced photodegradation could be ascribed to the introduction of Au NPs in favor of promoting the separation process of the photogenerated e^-/h^+ pairs. Furthermore, the antimicrobial assays show good antimicrobial activity for both pure ZnO and Au/ZnO samples for *E. coli* bacteria. In which, Au/ZnO-Hg lamp exhibited the best antibacterial efficiency. The antibacterial effect of the materials was also significantly enhanced by increasing the concentration of the test agent or increasing the Au content doped on ZnO. In summary, Au-doped ZnO has been proven to be a more excellent photocatalyst than undoped ZnO. Au/ZnO nanocomposite indeed has the potential for removing organic pollutants in wastewater and antimicrobial applications. Notwithstanding, depending on the intended use, the appropriate synthesis method can be selected.

CRediT Author Statement

Anh-Tuan Vu: Conceptualization, Experiment setup, material characterization of material, writing - review & editing, revision, supervision, project administration, Validation; Thi Anh Tuyet Pham: Research ideas, synthesis of material, studying the effects of reaction conditions on TA decomposition, collection of results, and writing the manuscript.

References

[1] Ngoc, K.H.P., Vu, A.-T. (2022). Simple Preparation of the $CuO \cdot Fe_3O_4$/Silica Composite from Rice Husk for Enhancing Fenton-Like Catalytic Degradation of Tartrazine in a Wide pH Range. *Adsorption Science & Technology,* 2022, 6454354. DOI: 10.1155/2022/6454354.

[2] Madihi-Bidgoli, S., Asadnezhad, S., Yaghoot-Nezhad, A., Hassani, A. (2021). Azurobine degradation using Fe_2O_3@multi-walled carbon nanotube activated peroxymonosulfate (PMS) under UVA-LED irradiation: performance, mechanism and environmental application. *Journal of Environmental Chemical Engineering,* 9(6), 106660. DOI: 10.1016/j.jece.2021.106660.

[3] Hassani, A., Eghbali, P., Mahdipour, F., Wacławek, S., Lin, K.-Y.A., Ghanbari, F. (2023). Insights into the synergistic role of photocatalytic activation of peroxymonosulfate by UVA-LED irradiation over $CoFe_2O_4$-rGO nanocomposite towards effective Bisphenol A degradation: Performance, mineralization, and activation mechanism. *Chemical Engineering Journal*, 453, 139556. DOI: 10.1016/j.cej.2022.139556.

[4] Karim, A.V., Hassani, A., Eghbali, P., Nidheesh, P.V. (2022). Nanostructured modified layered double hydroxides (LDHs)-based catalysts: A review on synthesis, characterization, and applications in water remediation by advanced oxidation processes. *Current Opinion in Solid State and Materials Science,* 26(1), 100965. DOI: 10.1016/j.cossms.2021.100965.

[5] Juneja, S., Madhavan, A., Ghosal, A., Moulick, R.G., Bhattacharya, J. (2017). Synthesis of Graphenized Au/ZnO Plasmonic Nanocomposites for Simultaneous Sunlight mediated Photo-catalysis and Anti-microbial Activity. *Journal of Hazardous Materials*, 347, 378-389. DOI: 10.1016/j.jhazmat.2017.12.034.

[6] Vu, A.-T., Pham, T.A.T., Mac, V.H., Nguyen, T.H. (2021). Facile Controlling of the Physical Properties of Zinc Oxide and Its Application to Enhanced Photocatalysis. *Journal of Analytical Methods in Chemistry,* 2021, 5533734. DOI: 10.1155/2021/5533734.

[7] Thi, T.A.N., Vu, A.-T. (2022). Nanocomposite $ZnO/g\text{-}C_3N_4$ for Improved Degradation of Dyes under Visible Light: Facile Preparation, Characterization, and Performance Investigations. *Bulletin of Chemical Reaction Engineering & Catalysis,* 17 (2), 403-419. DOI: 10.9767/bcrec.17.2.13931.403-419.

[8] Pham, T.A.T., Tran, V.A., Le, V.D., Nguyen, M.V., Truong, D.D., Do, X.T., Vu, A.-T. (2020). Facile Preparation of ZnO Nanoparticles and Ag/ZnO Nanocomposite and Their Photocatalytic Activities under Visible Light. *International Journal of Photoenergy,* 2020, 8897667. DOI: 10.1155/2020/8897667.

[9] Tu, V.A., Tuan, V.A. (2018). A facile and fast solution chemistry synthesis of porous ZnO nanoparticles for high efficiency photodegradation of tartrazine. *Vietnam Journal of Chemistry* 56 (2), 214-219. DOI: 10.1002/vjch.201800016.

[10] Nguyen, T.H., Vu, A.-T., Dang, V.H., Wu, J.C.-S., Le, M.T. (2020). Photocatalytic Degradation of Phenol and Methyl Orange with Titania-Based Photocatalysts Synthesized by Various Methods in Comparison with ZnO–Graphene Oxide Composite. *Topics in Catalysis,* 63, 1215–1226. DOI: 10.1007/s11244-020-01361-5.

[11] Joshi, K.M., Shrivastava, V.S. (2011). Photocatalytic degradation of Chromium(VI) from wastewater using nanomaterials like TiO2, ZnO, and CdS. *Applied Nanoscience* 1(3), 147-155. DOI: 10.1007/s13204-011-0023-2.

[12] Shirzad-Siboni, M., Farrokhi, M., Soltani, R.D.C., Khataee, A., Tajassosi, S. (2014). Photocatalytic Reduction of Hexavalent Chromium over ZnO Nanorods Immobilized on Kaolin. *Industrial & Engineering Chemistry Research,* 53(3), 1079-1087. DOI: 10.1021/ie4032583.

[13] Wang, Y., Zhang, L., Teng, B., Fan, M. (2015). High-efficiency conversion of CO_2 to fuel over $ZnO/g\text{-}C_3N_4$ photocatalyst. *Applied Catalysis B: Environmental,* 168-169, 1-8. DOI: 10.1016/j.apcatb.2014.12.017.

[14] Hassani, A., Faraji, M., Eghbali, P. (2020). Facile fabrication of mpg-C_3N_4/Ag/ZnO nanowires/Zn photocatalyst plates for photodegradation of dye pollutant. *Journal of Photochemistry and Photobiology A: Chemistry,* 400, 112665. DOI: 10.1016/j.jphotochem.2020.112665.

[15] Deng, Q., Duan, X., Ng, D.H.L., Tang, H., Yang, Y., Kong, M., Wu, Z., Cai, W., Wang, G. (2012). Ag Nanoparticle Decorated Nanoporous ZnO Microrods and Their Enhanced Photocatalytic Activities. *ACS Applied Materials & Interfaces,* 4 (11), 6030-6037. DOI: 10.1021/am301682g.

[16] Lee, J., Shim, H.S., Lee, M., Song, J.K., Lee, D. (2011). Size-Controlled Electron Transfer and Photocatalytic Activity of ZnO–Au Nanoparticle Composites. *The Journal of Physical Chemistry Letters,* 2 (22), 2840-2845. DOI: 10.1021/jz2013352.

[17] Udawatte, N., Lee, M., Kim, J., Lee, D. (2011). Well-Defined Au/ZnO Nanoparticle Composites Exhibiting Enhanced Photocatalytic Activities. *ACS Applied Materials & Interfaces,* 3 (11), 4531-4538. DOI: 10.1021/am201221x.

[18] Jaramillo-Páez, C.A., Navío, J.A., Hidalgo, M.C., Macías, M. (2018). ZnO and Pt-ZnO photocatalysts: Characterization and photocatalytic activity assessing by means of three substrates. *Catalysis Today,* 313, 12-19. DOI: 10.1016/j.cattod.2017.12.009.

[19] Mendoza-Mendoza, E., Nuñez-Briones, A.G., García-Cerda, L.A., Peralta-Rodríguez, R.D., Montes-Luna, A.J. (2018). One-step synthesis of ZnO and Ag/ZnO heterostructures and their photocatalytic activity. *Ceramics International,* 44 (6), 6176-6180. DOI: 10.1016/j.ceramint.2018.01.001.

[20] Lam, S.-M., Quek, J.-A., Sin, J.-C. (2018). Mechanistic investigation of visible light responsive Ag/ZnO micro/nanoflowers for enhanced photocatalytic performance and antibacterial activity. *Journal of Photochemistry and Photobiology A: Chemistry,* 353, 171-184. DOI: 10.1016/j.jphotochem.2017.11.021.

[21] Qi, K., Xing, X., Zada, A., Li, M., Wang, Q., Liu, S.-y., Lin, H., Wang, G. (2020). Transition metal doped ZnO nanoparticles with enhanced photocatalytic and antibacterial performances: Experimental and DFT studies. *Ceramics International,* 46 (2), 1494-1502. DOI: 10.1016/j.ceramint.2019.09.116.

[22] Wang, G., Zhang, L., Li, Y., Zhao, W., Kuang, A., Li, Y., Xia, L., Li, Y., Xiao, S. (2020). Biaxial strain tunable photocatalytic properties of 2D ZnO/GeC heterostructure. *Journal of Physics D: Applied Physics,* 53(1), 015104. DOI: 10.1088/1361-6463/ab440e.

[23] Qi, K., Cheng, B., Yu, J., Ho, W. (2017). Review on the improvement of the photocatalytic and antibacterial activities of ZnO. *Journal of Alloys and Compounds*, 727, 792-820. DOI: 10.1016/j.jallcom.2017.08.142.

[24] Mohd Yusof, H., Mohamad, R., Zaidan, U.H., Abdul Rahman, N.A. (2019). Microbial synthesis of zinc oxide nanoparticles and their potential application as an antimicrobial agent and a feed supplement in animal industry: a review. *Journal of Animal Science and Biotechnology*, 10 (1), 57. DOI: 10.1186/s40104-019-0368-z.

[25] Shim, K., Abdellatif, M., Choi, E., Kim, D. (2017). Nanostructured ZnO films on stainless steel are highly safe and effective for antimicrobial applications. *Applied Microbiology and Biotechnology*, 101 (7), 2801-2809. DOI: 10.1007/s00253-017-8099-6.

[26] Janaki, A.C., Sailatha, E., Gunasekaran, S. (2015). Synthesis, characteristics and antimicrobial activity of ZnO nanoparticles. *Spectrochimica Acta Part A: Molecular and Biomolecular Spectroscopy,* 144, 17-22. DOI: 10.1016/j.saa.2015.02.041.

[27] Kaushik, M., Niranjan, R., Thangam, R., Madhan, B., Pandiyarasan, V., Ramachandran, C., Oh, D.-H., Venkatasubbu, G.D. (2019). Investigations on the antimicrobial activity and wound healing potential of ZnO nanoparticles. *Applied Surface Science*, 479, 1169-1177. DOI: 10.1016/j.apsusc.2019.02.189.

[28] Ye, L., Cao, Z., Liu, X., Cui, Z., Li, Z., Liang, Y., Zhu, S., Wu, S. (2022). Noble metal-based nanomaterials as antibacterial agents. *Journal of Alloys and Compounds*, 904, 164091. DOI: 10.1016/j.jallcom.2022.164091.

[29] Gholap, H.M., Warule, S., Sangshetti, J., Kulkarni, G., Banpurkar, A., Satpute, S., Patil, R. (2016). Hierarchical nanostructures of Au@ZnO: antibacterial and antibiofilm agent. *Applied Microbiology and Biotechnology,* 100, 5849–5858. DOI: 10.1007/s00253-016-7391-1.

[30] Majhi, R.K., Mohanty, S., Khan, M.I., Mishra, A., Brauner, A. (2021). Ag@ZnO Nanoparticles Induce Antimicrobial Peptides and Promote Migration and Antibacterial Activity of Keratinocytes. *ACS Infectious Diseases,* 7(8), 2068-2072. DOI: 10.1021/acsinfecdis.0c00903.

[31] Vu, A.-T., Pham, T.A.T., Tran, T.T., Nguyen, X.T., Tran, T.Q., Tran, Q.T., Nguyen, T.N., Doan, T.V., Vi, T.D., Nguyen, C.L., Nguyen, M.V., Lee, C.-H. (2020). Synthesis of Nano-Flakes Ag・ZnO・Activated Carbon Composite from Rice Husk as A Photocatalyst under Solar Light. *Bulletin of Chemical Reaction Engineering & Catalysis*, 15(1), 264-279. DOI: 10.9767/bcrec.15.1.5892.264-279.

[32] Biswal, R., Yadav, P., Khan, B., Harish, H., Kumar, P., Singh, M.K. (2022). Synthesis and optical properties of citric acid (CA) doped $ZnFe_2O_4$ hybrid nanocomposite. *Materials Today: Proceedings,* 67, 145-150. DOI: 10.1016/j.matpr.2022.05.575.

[33] Zhou, H., Zhang, H., Wang, Y., Miao, Y., Gu, L., Jiao, Z. (2015). Self-assembly and template-free synthesis of ZnO hierarchical nanostructures and their photocatalytic properties. *Journal of Colloid and Interface Science,* 448, 367-373. DOI: 10.1016/j.jcis.2015.02.040.

[34] Qu, X., Yang, R., Tong, F., Zhao, Y., Wang, M.-H. (2018). Hierarchical ZnO microstructures decorated with Au nanoparticles for enhanced gas sensing and photocatalytic properties. *Powder Technology,* 330, 259-265. DOI: 10.1016/j.powtec.2018.02.019.

[35] Lin, Y., Wei, W., Wang, Y., Zhou, J., Sun, D., Zhang, X., Ruan, S. (2015). Highly stabilized and rapid sensing acetone sensor based on Au nanoparticle-decorated flower-like ZnO microstructures. *Journal of Alloys and Compounds,* 650, 37-44. DOI: 10.1016/j.jallcom.2015.07.242.

[36] Hameed, A.S.H., Karthikeyan, C., Ahamed, A.P., Thajuddin, N., Alharbi, N.S., Alharbi, S.A., Ravi, G. (2016). In vitro antibacterial activity of ZnO and Nd doped ZnO nanoparticles against ESBL producing Escherichia coli and Klebsiella pneumoniae. *Scientific Reports,* 6(1), 24312. DOI: 10.1038/srep24312.

[37] Ahmad, M., Rehman, W., Khan, M.M., Qureshi, M.T., Gul, A., Haq, S., Ullah, R., Rab, A., Menaa, F. (2021). Phytogenic fabrication of ZnO and gold decorated ZnO nanoparticles for photocatalytic degradation of Rhodamine B. *Journal of Environmental Chemical Engineering,* 9(1), 104725. DOI: 10.1016/j.jece.2020.104725.

[38] Lei, C., Pi, M., Jiang, C., Cheng, B., Yu, J. (2017). Synthesis of hierarchical porous zinc oxide (ZnO) microspheres with highly efficient adsorption of Congo red. *Journal of Colloid and Interface Science,* 490, 242-251. DOI: 10.1016/j.jcis.2016.11.049.

[39] Gavade, N.L., Kadam, A.N., Babar, S.B., Gophane, A.D., Garadkar, K.M., Lee, S.-W. (2020). Biogenic synthesis of gold-anchored ZnO nanorods as photocatalyst for sunlight-induced degradation of dye effluent and its toxicity assessment. *Ceramics International,* 46 (8, Part A), 11317-11327. DOI: 10.1016/j.ceramint.2020.01.161.

[40] Babu, K.S., Reddy, A.R., Sujatha, C., Reddy, K.V., Mallika, A.N. (2013). Synthesis and optical characterization of porous ZnO. *Journal of Advanced Ceramics,* 2(3), 260-265. DOI: 10.1007/s40145-013-0069-6.

[41] Bouzid, H., Faisal, M., Harraz, F.A., Al-Sayari, S.A., Ismail, A.A. (2015). Synthesis of mesoporous Ag/ZnO nanocrystals with enhanced photocatalytic activity. *Catalysis Today,* 252, 20-26. DOI: 10.1016/j.cattod.2014.10.011.

[42] Ismail, A.A., Harraz, F.A., Faisal, M., El-Toni, A.M., Al-Hajry, A., Al-Assiri, M.S. (2016). A sensitive and selective amperometric hydrazine sensor based on mesoporous Au/ZnO nanocomposites. *Materials & Design,* 109, 530-538. DOI: 10.1016/j.matdes.2016.07.107.

[43] Zheng, X., Zhang, Z., Meng, S., Wang, Y., Li, D. (2020). Regulating charge transfer over 3D Au/ZnO hybrid inverse opal toward efficiently photocatalytic degradation of bisphenol A and photoelectrochemical water splitting. *Chemical Engineering Journal,* 393, 124676. DOI: 10.1016/j.cej.2020.124676.

[44] Jin, Y., Jiao, S., Lu, H., Wang, D., Gao, S., Wang, J. (2020). Localized Surface Plasmon-Enhanced Ultraviolet and Visible Photoresponse Based on ZnO Films with Au Nanoparticles. *Journal of Electronic Materials,* 49(8), 4491-4497. DOI: 10.1007/s11664-020-08153-3.

[45] Lu, J., Wang, H., Peng, D., Chen, T., Dong, S., Chang, Y. (2016). Synthesis and properties of Au/ZnO nanorods as a plasmonic photocatalyst. *Physica E: Low-dimensional Systems and Nanostructures,* 78, 41-48. DOI: 10.1016/j.physe.2015.11.035.

[46] Yu, H., Ming, H.A.I., Gong, J., Li, H., Huang, H.U.I., Pan, K., Liu, Y., Kang, Z., Wei, J.I.E., Wang, D. (2013). Facile synthesis of Au/ZnO nanoparticles and their enhanced photocatalytic activity for hydroxylation of benzene. *Bulletin of Materials Science*, 36(3), 367-372. DOI: 10.1007/s12034-013-0491-y.

[47] Daud, S.N.H., Haw, C.Y., Chiu, W.S., Aspanut, Z., Jani, N.A., Khiew, P.S., Lim, Y.C., Abd. Hamid, M.A., Ali, A.M. (2017). 3D hyperbranched heterostructures of Ag nanocrystals-decorated ZnO nanopillars: controlled growth and characterization of the optical properties. *CrystEngComm,* 19(37), 5591-5603. DOI: 10.1039/C7CE01159H.

[48] Wu, G., Zhao, G., Sun, J., Cao, X., He, Y., Feng, J., Li, D. (2019). The effect of oxygen vacancies in ZnO at an Au/ZnO interface on its catalytic selective oxidation of glycerol. *Journal of Catalysis*, 377, 271-282. DOI: 10.1016/j.jcat.2019.06.030.

[49] Liu, X., Liu, M.-H., Luo, Y.-C., Mou, C.-Y., Lin, S.D., Cheng, H., Chen, J.-M., Lee, J.-F., Lin, T.-S. (2012). Strong Metal–Support Interactions between Gold Nanoparticles and ZnO Nanorods in CO Oxidation. *Journal of the American Chemical Society,* 134(24), 10251-10258. DOI: 10.1021/ja3033235.

[50] Vu, A.-T., Pham, T.A.T., Do, X.T., Tran, V.A., Le, V.D., Truong, D.D., Nguyen, T.H., Nguyen, M.V. (2021). Preparation of Hierarchical Structure Au/ZnO Composite for Enhanced Photocatalytic Performance: Characterization, Effects of Reaction Parameters, and Oxidizing Agent Investigations. *Adsorption Science & Technology,* 2021, 5201497. DOI: 10.1155/2021/5201497.

[51] Choudhary, M.K., Kataria, J., Sharma, S. (2018). Novel Green Biomimetic Approach for Preparation of Highly Stable Au-ZnO Heterojunctions with Enhanced Photocatalytic Activity. *ACS Applied Nano Materials,* 1(4), 1870-1878. DOI: 10.1021/acsanm.8b00272.

[52] Song, X., Liu, Y., Zheng, Y., Ding, K., Nie, S., Yang, P. (2016). Synthesis of butterfly-like ZnO nanostructures and study of their self-reducing ability toward Au3+ ions for enhanced photocatalytic efficiency. *Physical Chemistry Chemical Physics,* 18(6), 4577-4584. DOI: 10.1039/C5CP07187A.

[53] He, W., Kim, H.-K., Wamer, W.G., Melka, D., Callahan, J.H., Yin, J.-J. (2014). Photogenerated Charge Carriers and Reactive Oxygen Species in ZnO/Au Hybrid Nanostructures with Enhanced Photocatalytic and Antibacterial Activity. *Journal of the American Chemical Society*, 136(2), 750-757. DOI: 10.1021/ja410800y.

[54] Awad, A., Abou-Kandil, A.I., Elsabbagh, I., Elfass, M., Gaafar, M., Mwafy, E. (2015). Polymer nanocomposites part 1:Structural characterization of zinc oxide nanoparticles synthesized via novel calcination method. *Journal of Thermoplastic Composite Materials*, 28(9), 1343-1358. DOI: 10.1177/0892705714551241.

[55] Seil, J.T., Webster, T.J. (2012). Antimicrobial applications of nanotechnology: methods and literature, *International Journal of Nanomedicine*, 7, 2767-2781. DOI: 10.2147/IJN.S24805.

[56] Hitkari, G., Chowdhary, P., Kumar, V., Singh, S., Motghare, A. (2022). Potential of Copper-Zinc Oxide nanocomposite for photocatalytic degradation of congo red dye. *Cleaner Chemical Engineering,* 1, 100003. DOI: 10.1016/j.clce.2022.100003.

[57] Bhushan, B., Jahan, K., Verma, V., Murty, B.S., Mondal, K. (2020). Photodegradation of methylene blue dye by powders of Ni–ZnO floweret consisting of petals of ZnO nanorod around Ni-rich core. *Materials Chemistry and Physics*, 253, 123394. DOI: 10.1016/j.matchemphys.2020.123394.

[58] Bouarroudj, T., Aoudjit, L., Djahida, L., Zaidi, B., Ouraghi, M., Zioui, D., Mahidine, S., Shekhar, C., Bachari, K. (2021). Photodegradation of tartrazine dye favored by natural sunlight on pure and (Ce, Ag) co-doped ZnO catalysts. *Water Science and Technology*, 83(9), 2118-2134. DOI: 10.2166/wst.2021.106.